https://doi.org/10.5194/egusphere-2025-2440
Preprint. Discussion started: 17 June 2025

A Simplified Relationship Between the Zero-percolation Threshold and Fracture Set Properties

Shaoqun Dong[1,2,3*], Lianbo Zeng[1,4], Chaoshui Xu[3], Peter Dowd[3], Guohao Xiong[1,2],Tao Wang[5], Wenya Lyu[1,4]

[1] National Key Laboratory of Petroleum Resources and Engineering, China University of Petroleum (Beijing), Beijing, China. 102249

[2] College of Science, China University of Petroleum, Beijing, China 102249

[3] School of Civil, Environmental and Mining Engineering, University of Adelaide, Adelaide, Australia 5005

[4] College of Geosciences, China University of Petroleum, Beijing, China 102249

[5] Chinese Academy of Geological Sciences, Beijing, China 100037

Correspondence to: Shaoqun Dong (dshaoqun@163.com) ORCID: 0000-0001-8204-7336

Abstract. Percolation analysis is an efficient way of evaluating the connectivity of discrete fracture networks. Except for very simple cases, it is not feasible to use analytical approaches to find the percolation threshold of a discrete fracture network. The most commonly used percolation threshold corresponds to the occurrence of percolation on average for the set of parameters (p50), which is not adequate for applications in which a high confidence in the percolation threshold is required. This study investigates the direct relationships between the percolation threshold at low probability (p0, named as zero-percolation threshold) and the properties of fracture networks with one set of fractures (fractures with similar orientations) in two-demensional domains. A generalized non-linear multivariate relationship between p0 and fracture network parameters is established based on connectivity assessments of a significant number of numerical simulations of fracture networks. A feature of this relationship is the invariant shape of marginal relationships. A comparison study with an analytical solution and applications in both synthetic and real fracture networks show that the derived relationship performs well in fracture networks of different sizes and orientations. A significant benefit of this relationship is that, when an analytical solution is not available, it can provide fast and reliable connectivity statistics of fracture networks based only on fracture parameters.

Keywords: Percolation; percolation threshold; fracture network; connectivity; discrete fracture network.

1 Introduction

Discrete fracture networks (DFN) are widely used to model fracture systems in rock masses and reservoirs for flow analysis (Dogan, 2023; Kolyukhin, 2022; Liu et al., 2019). In three-dimensional DFNs, fractures are represented using simplified geometric shapes such as polygons, rectangles, disks, and others. In two-dimensional DFNs, fractures are simplified as line

https://doi.org/10.5194/egusphere-2025-2440
Preprint. Discussion started: 17 June 2025

segments (Dong et al., 2020). DFN models are generally considered to be more realistic representations of the fracture system and they are more amenable to integrating geological data into the flow model (Dong et al., 2018). Fracture connectivity analysis is a significant component in the DFN approach to assessing flow behaviour (Alghalandis et al., 2015; Einstein & Locsin, 2012) as the conductivities of fractures are generally magnitudes greater than those of the surrounding porous matrix (Thovert et al., 2017). A good understanding of the connectivity of fracture networks is essential for many applications such as oil and gas recovery, geothermal energy exploitation, hydrology and groundwater engineering, and geological storage of radioactive wastes.

Percolation theory (Jafari & Babadagli, 2013; Khamforoush & Shams, 2007; Or et al., 2023; Sun et al., 2023) provides a basis for describing and quantifying the connectivity of geometrically complex systems (Xu et al., 2007) such as fracture networks and this is reflected in many studies reported in the literature that use percolation theory in the connectivity analysis of fracture systems (Barker, 2018; de Dreuzy et al., 2000; Dong et al., 2022; Khamforoush & Shams, 2007; Manzocchi, 2002; Masihi & King, 2007; Mourzenko et al., 2012). Percolation describes the phenomenon in which there is at least one domain-spanning pathway in a physical system (Tang et al., 2022; Yao et al., 2020; Yi & Tawerghi, 2009). Percolation in a DFN involves at least one cluster of connected fractures that spans the reservoir (McKenna et al., 2020) or rock mass (one cluster refers to a series of fractures which intersects each other). In this context, one of the most important characteristics of a fracture network is whether or not it percolates (Bour & Davy, 1998; Bour & Davy, 1997) and the percolation threshold is commonly used to quantify the critical value of connectivity at which the network percolates (Khamforoush & Shams, 2007; Manzocchi et al., 2023; Walsh & Manzocchi, 2021). Using this definition, the permeability of a fracture network is zero if the connectivity value is less than the percolation threshold (Mourzenko et al., 2005).

The percolation threshold of a DFN is a property that depends on the parameters of the fracture system (Mourzenko et al., 2005). Features previously used to characterise percolation in DFNs include the dimensionless density derived from the excluded volume (Barker, 2018; de Dreuzy et al., 2000; Khamforoush et al., 2008; Mourzenko et al., 2012), fractal dimensions (Jafari & Babadagli, 2013; Jafari & Babadagli, 2009; Zhao et al., 2016), topological connectivity measures (Manzocchi, 2002), fracture clustering (Manzocchi, 2002), and the average number of intersections per fracture (Manzocchi, 2002). These indirect characteristics of DFN models are derived from direct fracture network parameters, such as the number of fractures, fracture locations, sizes, and orientations, which have a joint effect on the occurrence of a percolating network (Jafari & Babadagli, 2009). For example, if the fracture size is kept constant, an increase in the number of fractures will result in a higher fracture density, which in turn will increase the probability of a connected domain (Shokri et al., 2016).

There are many published studies on the percolation of DFN models, with different focuses on different aspects of the problem. For fracture locations, DFN models in these studies cover both the Poisson (homogeneous) distribution (Barker, 2018; Bour & Davy, 1997; de Dreuzy et al., 2000; Huseby & Thovert, 1997; Jafari & Babadagli, 2013; Khamforoush & Shams, 2007; Mourzenko et al., 2005; Robinson, 1983; Thovert et al., 2017; Zhao et al., 2009; Zhao et al., 2016) and non-homogeneous (i.e.,

https://doi.org/10.5194/egusphere-2025-2440
Preprint. Discussion started: 17 June 2025

spatially correlated) distributions (Manzocchi, 2002; Mourzenko et al., 2012). For fracture sizes, some DFNs use the monodisperse model, which means that the shape and size of every fracture is identical (Jafari & Babadagli, 2013; Khamforoush & Shams, 2007; Khamforoush et al., 2008; Manzocchi, 2002; Mourzenko et al., 2012; Robinson, 1983). This makes the percolation study relatively simple using numerical simulation. Others use the polydisperse model in which the sizes (Bour & Davy, 1997; Huseby & Thovert, 1997; Mourzenko et al., 2004; Mourzenko et al., 2005; Thovert et al., 2017; Zhao et al., 2016) and shapes (Barker, 2018; Thovert et al., 2017) of fractures are different. Commonly used fracture size distributions include the power law function (Mourzenko et al., 2004; Mourzenko et al., 2005; Zhao et al., 2016), exponential distribution (Catapano et al., 2023; Dowd et al., 2007; Fadakar Alghalandis, 2017; Xu et al., 2007; Zhu et al., 2022) and uniform distribution (Huseby & Thovert, 1997). For fracture orientations, many DFNs use isotropic models (uniform and random) (Barker, 2018; Bour & Davy, 1997; Charlaix et al., 1984; de Dreuzy et al., 2000; Huseby & Thovert, 1997; Jafari & Babadagli, 2013; Khamforoush & Shams, 2007; Khamforoush et al., 2008; Mourzenko et al., 2004; Mourzenko et al., 2012; Mourzenko et al., 2005; Robinson, 1983; Thovert et al., 2017; Yi, Tawerghi, 2009; Zhao et al., 2016) but anisotropic (with a single preferential orientation or several preferential orientations) models are also commonly used (Balberg & Binenbaum, 1983; Khamforoush & Shams, 2007; Khamforoush et al., 2008; Manzocchi, 2002). The Fisher distribution (Khamforoush & Shams, 2007; Xu & Dowd, 2010) is the most commonly used type of distribution for three-dimensional fracture networks, while the von Mises distribution (Xu & Dowd, 2010) is the most commonly used for two-dimensional fracture networks. Physically, fractures related to tectonic movements are, in general, anisotropic (e.g., conjugate fractures generated around the maximum principal compressive stress (Zhao & Hou, 2017), while fractures associated with other causes, such as diagenesis, are typically isotropic (Dong et al., 2018).

A common method used to obtain the percolation threshold of a DFN is first to calculate some indirect characteristic parameters of the fracture network and then evaluate the percolation threshold on the basis of these parameters. However, DFNs with the same indirect characteristic parameters may have quite different direct geometrical parameters (e.g., number of fractures, fracture size, and orientation) and, unfortunately, these geometrical parameters dictate the fracture connectivity and hence the percolation threshold (Dong et al., 2019). For example, the two fracture networks in Figure 1 have the same number of fractures, identical fracture lengths, and box-counting fractal dimensions, but the network in Figure 1a percolates between side A and B, while the other (Figure 1b) does not percolate. The different orientations of these two fracture models lead to different percolation characteristics. In this case, the box-counting fractal dimension provides a good measure of the complexity of the system but it ignores the effect of the preferential orientation of a fracture network. Although the indirect approach can simplify the evaluation of the percolation threshold of a fracture network, it may sometimes produce misleading results. In addition, most percolation thresholds based on the excluded volume method correspond to the occurrence of percolation on average (Barker, 2018; Yi & Tawerghi, 2009) (i.e., with 50% probability, p50) due to the stochastic nature of fracture networks (c.f. Section 2.2). The level of confidence in such thresholds may not be sufficient for some applications. For example, for

https://doi.org/10.5194/egusphere-2025-2440
Preprint. Discussion started: 17 June 2025

underground radioactive waste storage facilities, selecting storage sites that minimize the potential number of connected pathways to the biosphere is important. In this case, a low probability percolation threshold (p0, c.f., Section 2.2) named as zero-percolation threshold is more important for the connectivity analysis of the fracture systems (Dong et al., 2019).

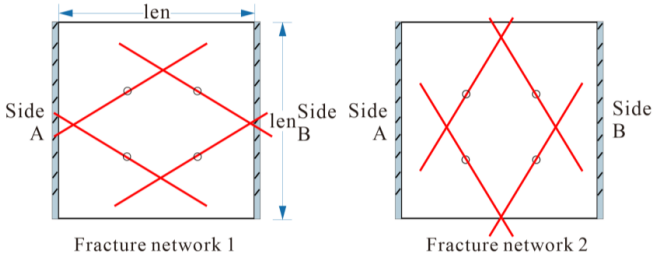

(a) Percolated DFN (b) Un-percolated DFN

Figure 1: Schematic diagram of two DFN models with different percolation features.

In practical engineering applications, it would be less problematic to use the direct relationship between the percolation threshold and fracture network parameters for connectivity assessments instead of resolving the problem by numerical simulations in every case. In general, it is not possible to establish such a relationship analytically due to the complexity of DFNs. In this work, Monte Carlo simulations of the number of fractures, n, fracture size (length), L ,and fracture orientation, ϕ are used to establish this relationship for two-dimensional DFN models, the fractures are represented by vectors representing line segments (Dong et al., 2020). In particular, fracture locations follow the Poisson distribution, fracture lengths follow the exponential distribution $f(L|\lambda)$, and fracture orientations follow the von-Mises distribution $f(\phi|\mu,\kappa)$, where λ, μ and κ are their corresponding distribution parameters (see Section 2.1). The zero-percolation threshold (p0) equation $L_t = f(n,\mu,\kappa)$ was established by analysing results from an extensive set of numerical simulations for fracture networks with one set of fractures (fractures that exhibit similar orientations) (Ali & Jakobsen, 2011; Zeng et al., 2022) (see Sections 3.1-3.2). Besides DFN with exponential fracture length, given the widespread adoption of lognormal distribution $f(L|\mu,\sigma)$ in characterizing fracture length distributions within DFN, it is imperative to explore the implications of this distribution on the phenomenon of zero-percolation. Here, μ,σ are parameters in lognormal distribution. Consequently, this paper extends its investigation beyond DFNs employing exponential distribution for fracture lengths to encompass those utilizing lognormal distribution, as detailed in Sections 3.3-3.4.

The relationship was established by using a non-linear, multivariate fitting method for a relationship with invariant shapes of marginal functions; this is demonstrated by a simple example in Sections 2.2 and 2.3. The verification of the derived equations for zero-percolation will undergo a comprehensive series of tests in Section 4.

https://doi.org/10.5194/egusphere-2025-2440
Preprint. Discussion started: 17 June 2025

2 Principle of the mathematical method

To mitigate ambiguity, the mathematical approach will utilise DFN with exponential distributions as an instance to elucidate the fundamental principles. Fracture parameters of a DFN model are described in Section 2.1. The percolation and percolation threshold of a DFN are described in Section 2.2. In Section 2.3, the non-linear fitting method is illustrated using a simple percolation example.

2.1 Discrete fracture networks

DFN modelling is a stochastic simulation method that uses marked point processes (MPP) (Dong et al., 2018c) in which fracture location (x, y) is modelled by a point process (Figure 2a) following a Poisson, non-homogeneous cluster or Cox point process (Mardia et al., 2007); and fracture properties (such as length L, orientation ϕ) are modelled at each point by marks (Figure 2b) following their respective probability distribution functions (e.g., $f(L)$ and $f(\phi)$) (Dong et al., 2018; Fadakar Alghalandis, 2017; Xu & Dowd, 2010). To simulate a set of n fractures with similar orientations, the location of a fracture (Figure 2a) is generated first followed by the generation of the associated marks (Figure 2b). Subsequently, these procedures are iterated *n* times to culminate in the ultimate implementation of the DFN (Figure 2c).

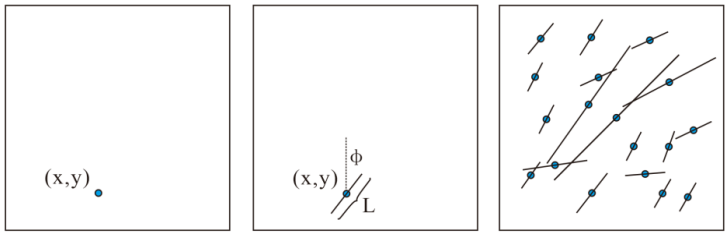

(a) Point process (b) Mark generation (c) Discrete fracture network

Figure 2: Schematic diagram of a two-dimensional DFN realisation. (a) Randomly generated fracture location; (b) Fracture properties (length, orientation) are generated from their probability distributions; (c) Repeat process (a) and (b) to generate the entire fracture network to account for the number of fractures in each fracture set as well as the number of fracture sets.

For 2D DFN models, fracture network parameters include the number of fracture sets, number of fractures n in each fracture set, fracture size distribution $f(L)$ and fracture orientation distribution $f(\phi)$. The study area used in this work is $100m \times 100m$ so $P20 = n_i \times 10^{-4}(m^{-2})$. Here, P20 is the fracture number per 2D unit area (Khamforoush et al., 2008). For fracture length, a fixed size L can be used, or the following exponential distribution (Xu & Dowd, 2010) is commonly used:

https://doi.org/10.5194/egusphere-2025-2440
Preprint. Discussion started: 17 June 2025

$$f(L|\lambda) = \begin{cases} \lambda e^{-\lambda L} & L \geq 0 \\ 0 & L < 0 \end{cases}, \quad (1)$$

where λ is the distribution parameter and therefore the average length, which in this case is $\bar{L} = 1/\lambda$. For fracture orientation, a von-Mises distribution (Fadakar Alghalandis, 2017; Xu & Dowd, 2010) is commonly used for 2D applications:

$$f(\phi|\mu,\kappa) = \frac{e^{\kappa cos\,(\phi-\mu)}}{2\pi I_0(\kappa)}, \quad (2)$$

where μ and κ are the distribution parameters, I_0 is the modified Bessel function defined as: $I_0(\kappa) = \sum_{i=0}^{+\infty} \frac{\kappa^{2i}}{2^{2i}(i!)^2}$.

μ and $1/\kappa$ are analogous to the mean and variance of a Gaussian distribution. μ represents the main fracture orientation. For example, in both Figure 3a and Figure 3b, the main orientation is NE-SW (Figure 3e and Figure 3f) so $\mu = \pi/4$, while in Figure 3c and Figure 3d, $\mu = \pi/2$ (Figure 3g and Figure 3h), following the common practice in geotechnical applications of measuring the bearing angle from the North. κ is a measure of concentration (reciprocal of the measure of dispersion). A comparison of Figure 3a and Figure 3c with Figure 3b and Figure 3d shows that the dispersion of the fracture orientation increases as $1/\kappa$ increases. When $\kappa = 0$, the distribution of fracture orientations is completely random. The DFN models were generated by a Matlab code based on the open-source toolbox ADFNE (Fadakar Alghalandis, 2017).

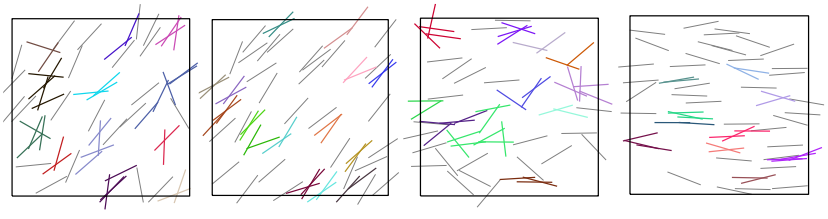

(a) $\mu = \pi/4$ $\kappa = 4$ (b) $\mu = \pi/4$ $\kappa = 24$ (c) $\mu = \pi/2$ $\kappa = 4$ (d) $\mu = \pi/2$ $\kappa = 24$

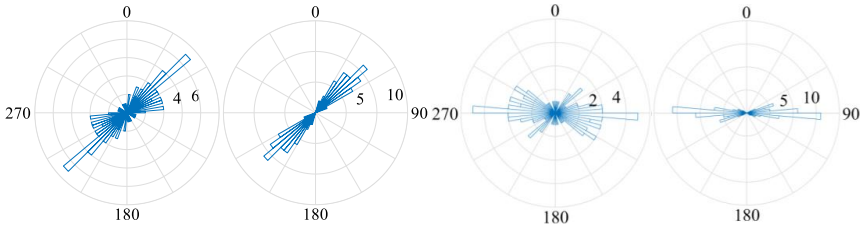

(e) $\mu = \pi/4$ $\kappa = 4$ (f) $\mu = \pi/4$ $\kappa = 24$ (g) $\mu = \pi/2$ $\kappa = 4$ (h) $\mu = \pi/2$ $\kappa = 24$

Figure 3. DFN models showing different fracture orientations with different μ, κ, together with their corresponding rose diagrams. Fractures of the same colour in the DFN model are in the same cluster, while fractures in black are isolated ones.

2.2 Percolation threshold of DFN models

Percolation in a DFN means there is at least one cluster of fractures spanning the system (rock mass or reservoir) that allows

https://doi.org/10.5194/egusphere-2025-2440
Preprint. Discussion started: 17 June 2025

the fluid to permeate from one side to the other, as shown in Figure 4b, while Figure 4a shows a non-percolating DFN. Obviously, one can easily conclude that an increase in fracture number or fracture size can lead to the percolation of the system at some stage. In reality, the probability of percolation is a function of many different factors related to the DFN parameters (Khamforoush et al., 2008), of which fracture density (such as P20 and P21 for 2D and P30 and P32 for 3D applications) is the most critical. Here, P21 is the fracture length per 2D unit area, while P30 and P32 are the fracture number and area per 3D unit volume, respectively.

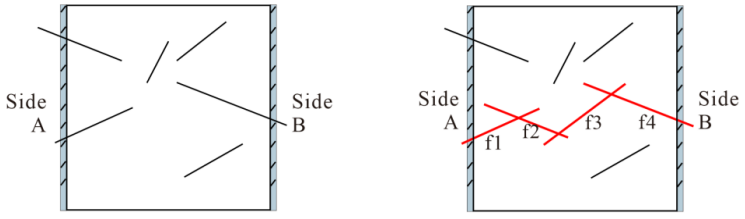

(a) Un-percolated DFN (b) Percolated DFN

Figure 4: Schematic diagram of percolation in DFN models.

For simple fracture networks, the percolation thresholds can be found analytically. However, for most fracture networks, approaches such as Monte Carlo (MC) simulation are required (Yi, Tawerghi, 2009). Due to the random nature of a DFN model, its corresponding percolation status is also stochastic in nature. If N independent simulations of a DFN are repeated for a group of parameters (n, L, ϕ), resulting in N_p number of cases where the fracture network percolates, then the percolation probability corresponding to the parameter set is $P = N_p/N$ (Barker, 2018; Yi & Tawerghi, 2009). In this work, p0, p50 ,and p100 represent the percolation probability of the DFN at $P = 0$, 50% and 100%, respectively. Note in stochastic systems, P = 0% and 100% may not be strictly possible and therefore the definition used here means the probability calculated by N_p/N using a reasonable number N (= 20 in this study). For stochastic systems, Figure 5 shows a worked example, in which the fracture orientations follow a von-Mises distribution ($\mu = 90°, \kappa = 24$) and fracture lengths are identical for each DFN. Twenty MC simulations ($N = 20$) were conducted using pairs of parameters ($n = 20,30,40, \ldots ,250$ and $L = 0.06,0.08,0.1, \ldots 0.8$). The percolation probability, P, calculated from the simulations, is shown in Figure 5, where the horizontal axes correspond to the number of fractures n and the fracture length L, respectively, and the z axis is the percolation probability of the corresponding DFN model.

https://doi.org/10.5194/egusphere-2025-2440
Preprint. Discussion started: 17 June 2025

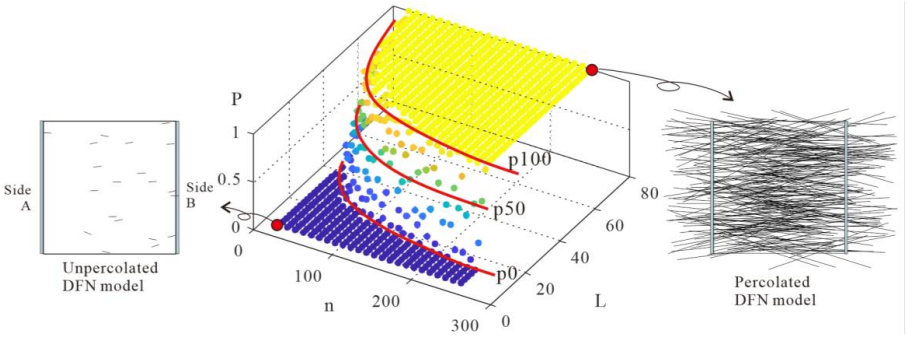

Figure 5: P vs. n and L for DFN models when fracture orientations are random and fracture lengths are identical in each DFN. Each point is obtained by 400 times simulations, and in other words, one pair of (n, L, P) can be obtained via 20 MC simulations, and each of MC simulation is repeated 20 times and then averaged.

Percolation threshold assessment is related to the percolation probability discussed above. As shown in Figure 5, there is a transition band between cases where the DFN is absolutely non-percolating ($P = 0$) and percolating ($P = 1$). The definition of percolation threshold should, therefore, consider the application context that defines the acceptance level of the percolation probability. For example, when it comes to subterranean repositories for radioactive waste, the selection of storage locations that mitigate the likelihood of interconnecting pathways to the biosphere and geo-spheres (e.g., aquifer systems) is of paramount importance (Wei et al., 2017; Yi & Tawerghi, 2009). In this case, the percolation threshold should be defined as that corresponding to a percolation probability of 0. On the other hand, for energy resource extraction (e.g., unconventional gas and enhanced geothermal systems), full connectivity is critical and a fully percolated fracture network is desirable. In this case, the percolation threshold should be defined as that corresponding to a percolation probability of 1, or close to 1 (e.g., 95%). Although the definition of percolation threshold could differ for different applications, the assessment of its relationships with DFN properties will be the same. Thus, for the work presented in this paper, the percolation threshold is defined as the case in which the percolation probability is 0.

Figure 6a shows points close to percolation thresholds extracted from results similar to those of Figure 5 based on 20 MC simulations. In fact, 20×20=400 MC simulations are used to obtain each point to obtain a sample close to the real one. In order to reduce the computation cost, there are a few differences in fracture number n and length L compared with those in Figure 5., i.e., $n = round(10^j) = 22, 32, 45, \ldots, 251$, j= 1.35, 1.5, 1.65, …, 2.4, $L = 10^k$= 0.0316, 0.0322, 0.0327, …, 1, $k = -1.5, -1.4925, -1.485, \ldots, 0$. The corresponding non-linear percolation threshold curve based on least-squares regression is $L_t = 1.7518 \times n^{-0.4308}$ with a correlation coefficient of 0.9288. When the specific number n is considered, an increase in L results in percolation. In this context, we hold the fracture number n to determine the fracture length threshold (denoted as L_t) for zero probability percolation, hence the utilisation of L_t and n. Conversely, if the fracture length is fixed, L and n_t will be employed. This curve defines the percolation threshold in terms of parameter pairs of (n, L_t). The DFN corresponding to any combination of parameters below this curve, namely $L < L_t$, will have a percolation probability of 0. To assess the uncertainty

https://doi.org/10.5194/egusphere-2025-2440
Preprint. Discussion started: 17 June 2025

of this relationship, 20 groups of MC simulations as used in Figure 6a were employed to obtain the non-linear relationship with statistical dispersion and the results are shown in Figure 6b. The circles correspond to the averages of 20 groups of 20 MC simulations (Figure 6a) and the error bars represent two times the corresponding standard deviations. The fitted non-linear relationship based on least-squares regression of the average values is $L_t = 1.592 \times n^{-0.403}$ with a correlation coefficient is 0.993.

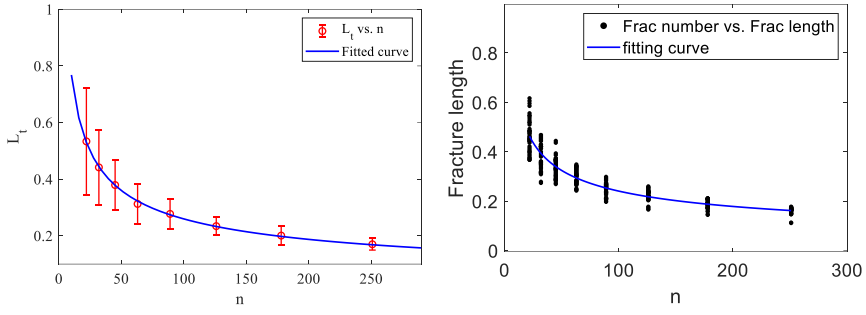

(a) Lt vs. n based on 20 MC simulations. The circle and half error bar represent average and two times standard deviation, respectively.

(b) Lt vs. n. Each black point is one average corresponding to a red circle in (a). For each n, 20 groups of 20 MCs are implemented.

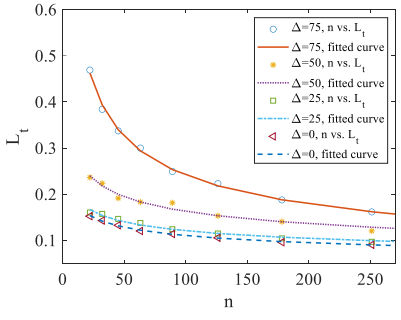

(c) Percolation threshold of (n, L_t) corresponding to different Δ.

Figure 6: Percolation threshold of (n, L_t) for the example DFN model.

Obviously, fracture orientations will also affect the percolation threshold curves. As an example to demonstrate these effects, the von-Mises distribution is used to describe the distribution of fracture orientations for the DFN model used above. In this case, the fracture network parameters are (n, L, μ, κ). To simplify the demonstration, the concentration parameter κ is set to 24, similar to those shown in Figure 3b and Figure 3d; μ is set to values from 90° to 0° in 5° decrements. As the horizontal percolation is of interest here, to simplify the comparison, μ is transformed to an angle measured from the horizontal direction, i.e., $\Delta = |\mu - 90|$, hence, $\Delta = 0°, 5°, \ldots, 90°$. The above curve fitting process was repeated and some results are

https://doi.org/10.5194/egusphere-2025-2440
Preprint. Discussion started: 17 June 2025

shown in Figure 6c. As Δ decreases, the percolation threshold decreases. This is consistent with the fact that lower Δ will increase the connectivity in the horizontal direction between the left and the right sides; percolation therefore requires a shorter fracture length and so the percolation threshold curve decreases.

2.3 Non-linear relationship for the percolation threshold

The general shapes of the percolation curves in Figure 6c can be considered to have similar shapes, which are represented as coloured curves in Figure 7. To understand further the relationship between L_t, n and Δ, average values of 20 MC simulations are shown in Figure 7. Coloured curves refer to slices of different n and Δ. The left colour curves are the variation of L_t and n with different values of Δ, and the right coloured curves are the variations of L_t and Δ with different values of n. Clearly, the threshold fracture length increases as the number of fractures decreases and the relative orientation Δ increases. This is because higher fracture density leads to greater percolation probability, a lower number of fractures requires longer fractures to maintain the same percolation probability.

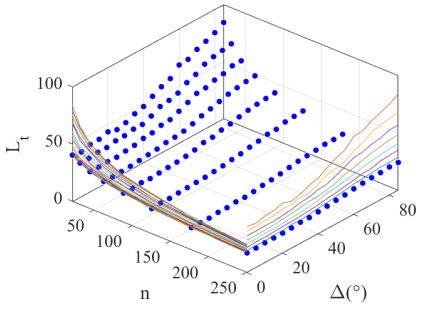

Figure 7: Simulated percolation threshold L_t vs. (n, Δ). For each pair of (n, Δ), 20 MC simulations are implemented to obtained the average L_t. Coloured curves are lines corresponding to slices of different n and Δ.

From the results in Figure 7, $L_t = f(n, \Delta)$ is non-linear. To establish this relationship, the variation of L_t with n for different values of Δ is examined first, i.e., $L_t = f_1(n)|_\Delta$, followed by assessing the influence of Δ on the derived $f_1(n)$ relationship. Note that at the second stage, $\cos\Delta$ is used instead of Δ as it is more relevant to the quantification of the fracture projection length in the horizontal direction ($len/\cos\Delta$).

Based on the simulation results discussed above, Eq. 5 is considered an appropriate fit to $f_1(n)$:

$$L_t = f_1(n) = an^b, \tag{5}$$

where a and b are parameters to be determined in the fitting process. The correlation coefficients for all curves for different Δ values (0°,5°…85°, 90°) are 0.9985,0.9895,…,0.9949, respectively. The high correlation coefficients (>0.96) confirm the suitability of using Eq. 5 to represent $f_1(n)$.

https://doi.org/10.5194/egusphere-2025-2440
Preprint. Discussion started: 17 June 2025

The relationships between a, b and $\cos\Delta$, shown in Figure 8, suggest linear relationships. Least squares regression was used to obtain the following equations:

$$a = a_1 cos^2\Delta + a_2 cos\Delta + a_3, \quad (6)$$

$$b = b_1 cos^2\Delta + b_2 cos\Delta + b_3, \quad (7)$$

with correlation coefficients of 0.9919 and 0.9712, respectively; $a_1, a_2, a_3, b_1, b_2, b_3$ are 2.726, -5.304, 2.887, -0.2552, 0.6134, and -0.5724, respectively.

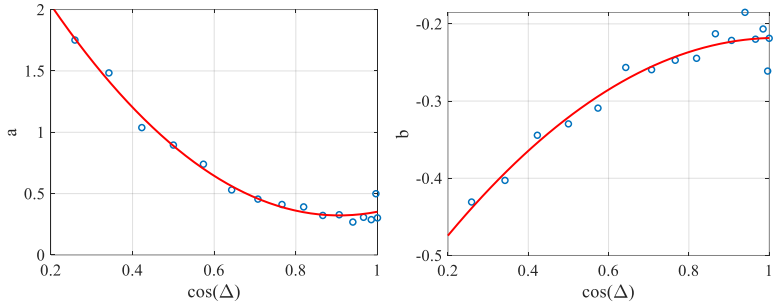

(a) a vs. $\cos\Delta$ (b) b vs. $\cos\Delta$

Figure 8: Influence of Δ on *a* and *b*.

By incorporating Eqs. 6 and 7 into Eq. 5 the final form of the expression of L_t in terms of the fracture network parameters is obtained, as shown in Eq. 8. This form is then used directly in a bivariate least squares fitting using the Levenberg-Marquardt algorithm (Ngia & Sjoberg, 2000), an optimal search technique for multivariate non-linear curve fitting. The original values of parameters shown in Eqs. 6 and 7 are used as initial inputs to the optimisation algorithm to improve computational efficiency and accuracy and the final derived parameters in this case are $(a_1, a_2, a_3, b_1, b_2, b_3) = (2.4757, -4.9064, 2.7359, -0.1841, 0.5097, -0.5336)$. This set of values should be a more accurate reflection of the bivariate relationship than the values obtained in the two separate consecutive steps described above.

$$\bar{L}_t = (a_1 cos^2\Delta + a_2 cos\Delta + a_3) n^{(b_1 cos^2\Delta + b_2 cos\Delta + b_3)}, \quad (8)$$

The final fitted surface is shown in Figure 9a. The points are the average values of 20 groups of MC simulation results shown in Figure 7. The suitability of the chosen functional form (Eq. 8) is confirmed by the fact that almost all the points are on the fitted surface. The plot in Figure 9b of simulated values of L_t against those predicted by Eq. 8 gives an extremely high correlation coefficient of nearly 1. It is also encouraging that, on visual inspection, the fitted curve is conditionally unbiased. Although this workflow is useful for multivariate non-linear fitting problems in which marginal relationships are of invariant

https://doi.org/10.5194/egusphere-2025-2440
Preprint. Discussion started: 17 June 2025

shape, it should be noted that difficulties may arise for very high dimensions (Dong et al., 2016).

The process described above can be summarised as an approach for fitting multiple variables. This approach starts by fitting a hypothetical relationship between L_t and n is initially fitted. Then, a new variable Δ is added by analysing relationships with the parameters in the hypothetical relationship model. The parameters in the hypothetical relationship model are then replaced by expressions of the newly added variable. Ultimately, the relationship between between L_t and (n, Δ) can be obtained. This approach will be applied in the relationship fitting of Section 3.2, where the independent variables are $(n, cos\Delta, \kappa)$.

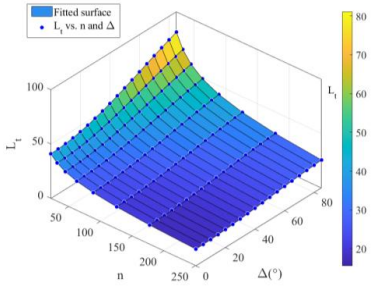

Fitted percolation threshold surface and simulation data

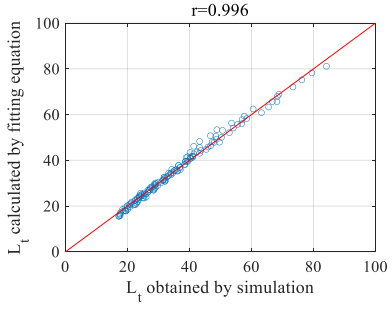

(b) Cross plot between simulated values of L_t and those predicted by Eq. 8

Figure 9: Bivariate percolation threshold fitting.

3 Percolation analysis of DFN models

3.1 Experiment design for DFN with exponential fracture lengths

In the example used above, the lengths and orientations are identical for all fractures in a fracture network, which is not generally the case in practical applications. The relationship described above can be made more useful by extending it to cover realistic fracture networks. The following numerical experiments were all implemented on a dimensionless unit square (1×1). Based on previously published work (Dong et al., 2018c; Xu et al., 2007), the lengths of rock fractures can generally be

https://doi.org/10.5194/egusphere-2025-2440
Preprint. Discussion started: 17 June 2025

modelled by an exponential or lognormal distribution. In this work, the exponential distribution was used and therefore the average length $\bar{L}$ is equal to $1/\lambda$ where λ is the distribution parameter. The von-Mises distribution (Eq. 2) was used for fracture orientation.

There are now three independent variables (n, Δ, κ) and the aim is to establish the relationship $\bar{L}_t = f(n, \Delta, \kappa)$. To simulate percolation states similar to those shown in Figure 5, DFNs corresponding to a combination of 8×18×13×200 (374,400) sets of variables are simulated and analysed, with each case simulated independently 20 times. The number of changes explored for each variable are listed in Table 1

Table 1.

Table 1: Parameters of DFNs in Section 3.2.

Parameter	Values analysed	Number of values
n	$round(10^i), i = 1.5,1.65,1.8,\ldots,2.4$	8
$\Delta = \lvert\mu - 90\rvert$	$(i-1)\times 5°, i = 1,2,3,\ldots,18$	18
κ	$round(10^i), i = 0.602,\ldots,2$	13
$\bar{L} = 1/\lambda$	$10^i, i = -1.5,-1.4925,-1.485,\ldots,0$	200

For each pair of (Δ, κ), 20 independent realisations of DFNs with different n and $\bar{L}$ were generated to obtain the percolation threshold curves $\bar{L}_t = f_1(n)$. These 20 MC simulations are used to calculate the percolation probability to obtain the points $(n, \bar{L}_t)$, as shown in Figure 10. The points are the average values of 20 groups of 20 MC simulations and the error bars represent two times of the corresponding standard deviation. The relationship in Eq. 5 was used again for $\bar{L}_t = f_1(n)|_{\Delta,\kappa}$. A comparison of Figure 6b and Figure 10 indicates that the standard deviations in this case are much larger, which is expected due to the variability in the lengths of fractures generated in simulations. Note that the uncertainty (reflected by the size of the error bar) increases as the number of fractures, n, decreases.

https://doi.org/10.5194/egusphere-2025-2440
Preprint. Discussion started: 17 June 2025

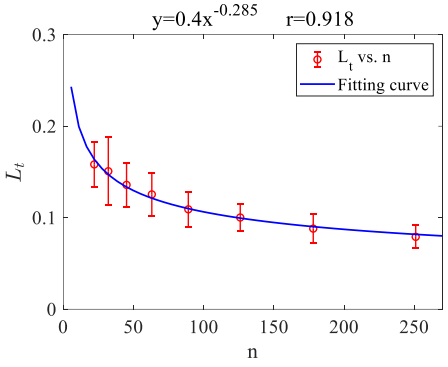

Figure 10: Variation of the percolation threshold as a function of n for $\kappa = 3$ and $\Delta = 0$.

3.2. Determining percolation threshold equation for DFN with exponential fracture length

Eq. 8 is only for a specific parameter κ. Establishing the full relationship, $\bar{L}_t = f(n, cos\Delta, \kappa)$, requires the relationships between $(a_1, a_2, a_3, b_1, b_2, b_3)$ in Eq. 8 and κ for different DFNs. The regression results for these parameters for different κ values are shown in Table 2, which provides the input data for the final non-linear fitting of the percolation threshold function. The correlation coefficients for each of the regressions in the table are all greater than 0.98, which ensures the suitability of the derived relationships.

Table 2: Regression parameters $(a_1, a_2, a_3, b_1, b_2, b_3)$ for different values of κ.

κ	a_1	a_2	a_3	b_1	b_2	b_3
3	30.1061	-0.3339	0.6003	-0.03176	0.08575	-0.329
6	0.3431	-0.8712	0.8535	-0.08643	0.2164	-0.3734
10	0.8132	-1.835	1.338	-0.1105	0.3005	-0.4269
13	1.328	-2.77	1.765	-0.1555	0.3679	-0.4494
18	1.883	-3.781	2.199	-0.2105	0.5097	-0.5119
24	2.726	-5.304	2.887	-0.2552	0.6134	-0.5724
32	3.212	-6.382	3.45	-0.3276	0.8044	-0.6671
56	6.14	-11.59	5.724	-0.2222	0.6696	-0.6211
75	8.671	-15.94	7.582	0.04139	0.3522	-0.5445

The relationships between a_1 and κ, between a_2 and κ and between a_3 and κ are linear as described by Eqs. 9-11; the relationship between b_1 and κ, between b_2 and κ and between b_3 and κ are quadratic as shown in Eqs. 12- 14. The

https://doi.org/10.5194/egusphere-2025-2440
Preprint. Discussion started: 17 June 2025

correlation coefficients of this set of regression curves are all greater than 0.98. Overall, these variables display a clear and strong relationship that can be described by an appropriate functional form. Table 3 lists the constants in Eqs. 9-14 obtained by least squares regression.

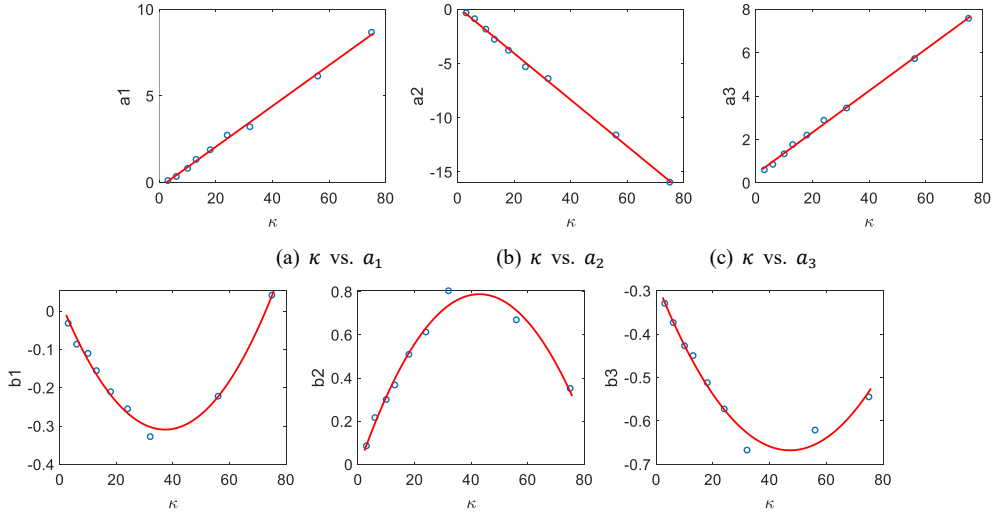

(a) κ vs. a_1 (b) κ vs. a_2 (c) κ vs. a_3

(d) κ vs. b_1 (e) κ vs. b_2 (f) κ vs. b_3

Figure 11: Relationship between κ and fitted parameters ($a_1, a_2, a_3, b_1, b_2, b_3$).

$$a_1 = a_{11}\kappa + a_{12}, \quad (9)$$

$$a_2 = a_{21}\kappa + a_{22}, \quad (10)$$

$$a_3 = a_{31}\kappa + a_{32}, \quad (11)$$

$$b_1 = b_{11}\kappa + b_{12}\kappa^2 + b_{13}, \quad (12)$$

$$b_2 = b_{21}\kappa + b_{22}\kappa^2 + b_{23}, \quad (13)$$

$$b_3 = b_{31}\kappa + b_{32}\kappa^2 + b_{33}, \quad (14)$$

where $a_{11}, a_{12}, a_{21}, a_{22}, a_{31}, a_{32}, b_{11}, b_{12}, b_{13}, b_{21}, b_{22}, b_{23}, b_{31}, b_{32}, b_{33}$ are parameters.

Table 3: Parameters of Eqs. (9) - (14).

a_{11}	a_{12}	a_{21}	a_{22}	a_{31}	a_{32}	b_{11}	b_{12}
0.1177	-0.296	-0.2143	0.2192	0.096	0.4064	0.0002	-0.0182

https://doi.org/10.5194/egusphere-2025-2440
Preprint. Discussion started: 17 June 2025

b_{13}	b_{21}	b_{22}	b_{23}	b_{31}	b_{32}	b_{33}
0.0299	-0.0004	0.0377	-0.0204	0.0002	-0.0165	-0.279

Finally, the combined percolation equation $\bar{L}_t = f(n, cos\Delta, \kappa)$ can be obtained, as shown in Eq. 15. The correlation coefficient is again nearly 1 (0.99).

$$\bar{L}_t = \left((a_{11}\kappa+a_{12})x^2 + (a_{21}\kappa+a_{22})x + (a_{31}\kappa+a_{32})\right)n^{\left(\frac{(b_{11}\kappa+b_{12}\kappa^2+b_{13})x^2}{+(b_{21}\kappa+b_{22}\kappa^2+b_{23})x+b_{31}\kappa+b_{32}\kappa^2+b_{33}}\right)}, \quad (15)$$

where $x = \cos\Delta$.

Again, these parameters are used as the inputs for the final multivariate least squares optimisation based on the Levenberg-Marquardt algorithm using all the simulation results. The final optimised values of the parameters in Eq. 15 are shown in Table 4. These values are similar to the initial parameter values obtained by the step-wise fitting process described above but they have been refined by global optimisation. The correlation coefficient between the prediction and simulation values based on the initial parameters (Table 3) is only 0.43 due to the error propagation in the step-wise fitting process. After global optimisation, the correlation coefficient increases significantly to nearly 1 (0.99) based on the values listed in Table 4.

Table 4: Parameters of the percolation equation in terms of fracture properties.

a_{11}	a_{12}	a_{21}	a_{22}	a_{31}	a_{32}	b_{11}	b_{12}
0.0643	-0.1587	-0.1188	-0.5551	0.0549	0.9823	-0.1612	0.2501
b_{13}	b_{21}	b_{22}	b_{23}	b_{31}	b_{32}	b_{33}	
-0.0945	0.2633	-0.0657	0.1313	-0.2025	0.1519	-0.4730	

To visualize the relationships in Eq. 28, several surfaces of $\bar{L}_t$ vs (n, Δ) corresponding to different values κ (4, 18, 42 and 75) are shown in Figure 12. In general, higher κ values correspond to higher percolation threshold values. This is because higher κ values correspond to lower variation of fracture orientations, which leads to lower probabilities of fracture intersections. Consequently, this reduces the connectivity of the fracture network and hence longer fractures are needed to reach percolation.

https://doi.org/10.5194/egusphere-2025-2440
Preprint. Discussion started: 17 June 2025

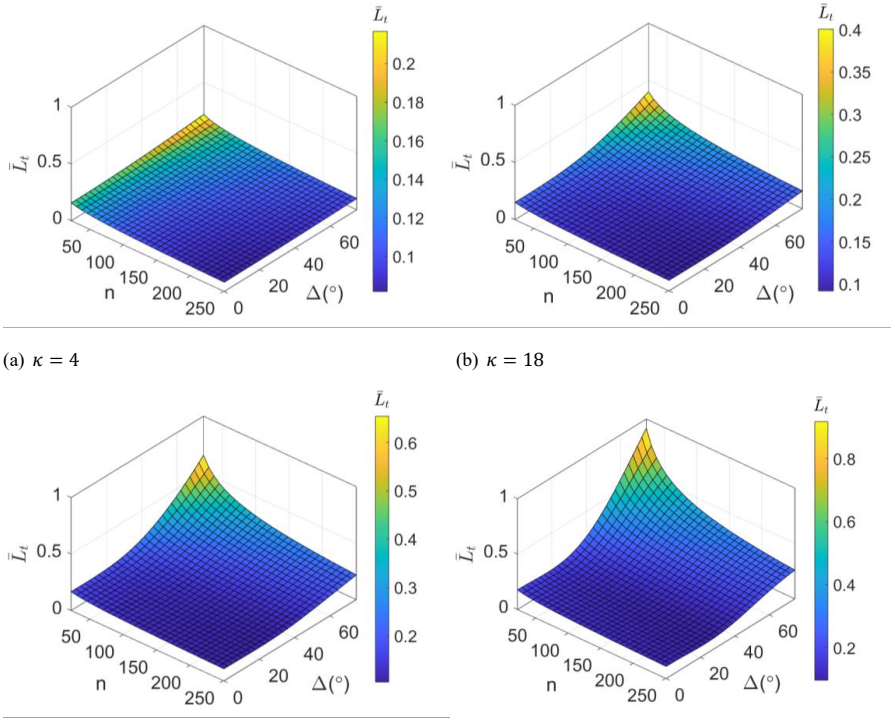

(a) $\kappa = 4$ (b) $\kappa = 18$

(c) $\kappa = 42$ (d) $\kappa = 75$

Figure 12: Extracted surfaces from the final percolation threshold equation.

Eq. 15 is derived for the region of a dimensionless unit square, the result is expected to be applicable to areas at different scales ($y \times y$). For these cases, the scaled percolation threshold $\bar{L}_{ts}$ will be used (Eq. 16) revised from Eq. 15. If the average fracture length of a fracture network $\bar{L} \geq \bar{L}_{ts}$, there is more probability reach percolation.

$$\bar{L}_{ts} = \bar{L}_t \times y, \tag{16}$$

3.3 Design of experiments for DFN with lognormal fracture lengths

In contrast to example used above, the length of rock fractures in this section is modelled using a lognormal distribution. The mean $\bar{L}$ and standard deviation v of fracture length are utilised to calculate the lognormal distribution parameters μ and σ as well as the probability density function, as shown in Eqs. 17-19. Five independent variables $(\bar{L}, v, \Delta, \kappa)$ are considered with the aim of establishing the relationship $n_t = f(\bar{L}, v, \Delta, \kappa)$. In this context, n_t represents the fracture number threshold at which the percolation threshold may be reached at a low probability (p0) in DFNs characterized by the parameters $(\bar{L}, v, \Delta, \kappa)$. In Section 3.1, the exponential distribution of fracture length is defined by a single parameter. Consequently, the fracture length is selected to determine the threshold corresponding to $p0$. Given that the fracture length is governed by two parameters $(\bar{L}, v)$, the parameters corresponding to the fracture length distribution are not selected. Instead, the fracture number is chosen.

https://doi.org/10.5194/egusphere-2025-2440
Preprint. Discussion started: 17 June 2025

$$\mu = \log(\bar{L}^2/\sqrt{\nu + \bar{L}^2}), \quad (17)$$

$$\sigma = \sqrt{\log(\nu / \bar{L}^2 + 1)}, \quad (18)$$

$$f(\bar{L}|\mu,\sigma) = \frac{1}{\bar{L}\sigma\sqrt{2\pi}} e^{\frac{-(\ln \bar{L}-\mu)^2}{2\sigma^2}}, \bar{L} > 0, \quad (19)$$

Simulations and analyses were conducted corresponding to the 8×6×6×18×13 (684,400) variable combinations for the DFNs, with each case independently simulated 20 times. The number of variations for each variable are listed in Table 5.

Table 5: Parameters of DFNs in Section 3.3.

Parameter	Values analysed	Number of values
n	$round(10^i), i = 1.5,1.65,1.8,\ldots,2.4$	8
$\bar{L}$	0.05,0.12,0.19,0.26,0.33,0.4	6
ν	2,4,6,8,10,12	6
$\Delta = \lvert\mu - 90\rvert$	$(i-1)\times 5°, i = 1,2,3,\ldots,18$	18
κ	$round(10^i), i = 0.602,\ldots,2$	13

3.4 Derivation of percolation threshold equation for DFN with lognormal fracture lengths

The multivariable fitting process for the DFN with lognormal fracture lengths is analogous to that described in Section 3.2. Initially, the hypothetical relationship between n_t and $\bar{L}$ is fitted (Eq. 20). Subsequently, by analysing the relationship between the parameters in the hypothetical model, new variables ν, Δ, and κ are sequentially incorporated. The expressions for the newly added variables are then used to replace the parameters in the hypothetical model. Ultimately, this yields the fitted relationship between n_t and $(\bar{L}, \nu, \Delta, \kappa)$, with the fitting process detailed in Eqs. 20-23, where $x = \cos\Delta$.

$$n_t = f(\bar{L}) = a\bar{L}^b + c, \quad (20)$$

$$n_t = f(\bar{L},\nu) = a_1 e^{a_2\nu}\bar{L}^{b_1} + c_1\nu^{c_2}, \quad (21)$$

$$n_t = f(\bar{L},\nu,\Delta) = (a_{11}x + a_{12})e^{a_{22}\nu}\bar{L}^{b_{11}x+b_{12}} + c_{11}\nu^{c_{12}x+c_{13}}, \quad (22)$$

$$n_t = f(\bar{L},\nu,\Delta,\kappa) = [(d_1\kappa^2+d_2\kappa+d_3)x + (d_4\kappa^2+d_5\kappa+d_6)]e^{\left(d_7\frac{\kappa}{\bar{L}}+d_8\right)\kappa\nu}\bar{L}^{d_9x_+^2d_{10}\kappa+d_{11}} + d_{12}\nu^{d_{13}x^2+d_{14}}, \quad (23)$$

Similarly, the parameters are used as inputs for the final multivariable least squares optimisation based on the Levenberg-Marquardt algorithm, utilising all simulation results. The final optimised values of the parameters in Eq. 23 are presented in Table 6.

https://doi.org/10.5194/egusphere-2025-2440
Preprint. Discussion started: 17 June 2025

417

418 **Table 6: Parameters of the percolation equation in terms of fracture properties.**

d_1	d_2	d_3	d_4	d_5	d_6	d_7
-0.0344	0.0560	0.2381	0.0335	0.0418	0.0053	-0.0002
d_8	d_9	d_{10}	d_{11}	d_{12}	d_{13}	d_{14}
0.0091	0.3048	0.0174	-1.4019	74.7657	-0.0001	0.0174

419

420 To visualise the relationships in Eq. 23, several surfaces of n_t vs $(\bar{L}, \nu, \Delta, \kappa)$ corresponding to different values of ν (2,
421 4, and 12) and κ (2, 7, and 10) are presented in Figure 13. Generally, higher Δ and lower $\bar{L}$ result in increased percolation
422 threshold n_t.

423

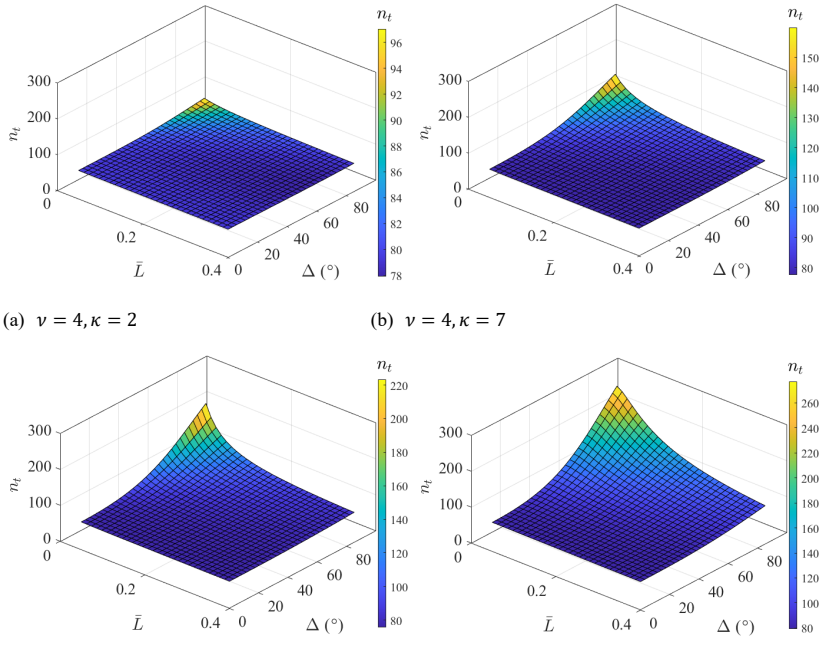

424

425 (a) $\nu = 4, \kappa = 2$ (b) $\nu = 4, \kappa = 7$

426

427 (c) $\nu = 2, \kappa = 10$ (d) $\nu = 12, \kappa = 10$

428 **Figure 13: Extracted surfaces from the final percolation threshold equation.**

429

430 Eq. 23 is derived for a dimensionless unit square, with its results expected to be applicable to regions of varying scales
431 $(y \times y)$. For these scenarios, the percolation threshold $\bar{n}_t$ will be adjusted using a scaling modification from Eq. 23, resulting
432 in Eq. 24. If the number of fractures N is more than $\bar{n}_{ts}$, the probability of achieving percolation will be high.

https://doi.org/10.5194/egusphere-2025-2440
Preprint. Discussion started: 17 June 2025

$$n_{ts} = n_t \times y_n, \quad (24)$$

where y_n is the scaling correction factor, $y_n = \log_{10}\left(\frac{1}{y} + 20\right)$.

4. Validation of the derived percolation threshold equation

4.1 Percolation analysis of fracture networks not used for deriving the threshold equation

(1) DFN with exponential fracture length. To test the performance of the derived zero percolation thresholds (Eq. 16), additional DFN models with different parameters ($n = 100{,}200, \Delta = 3°, 63°, \kappa = 5{,}40{,}50$) at different scales ($2m \times 2m$, $60m \times 60m$, $300m \times 300m$, $900m \times 900m$, $1100m \times 1100m$, $1200m \times 1200m$, $1300m \times 1300m$) were generated for percolation analysis. The percolation thresholds obtained from Eq. 16 and numerical simulation are shown in Figure 14. The close agreement between the predicted thresholds and the simulation results demonstrates that the derived relationships (Eq. 16) perform extremely well for predicting of zero percolation thresholds of DFNs with different parameters at different study scales.

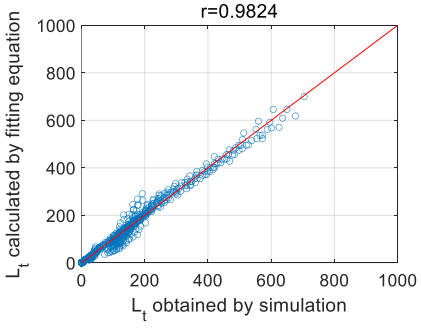

Figure 14: Validation of Eq. 16 in study areas on different scales.

(2) DFN with lognormal fracture length. To test the derived zero percolation thresholds (Eq. 24), additional DFN models with different parameters ($\bar{L} = 0.15{,}0.25$, $\nu = 5{,}7$, $\Delta = 26°, 56°$, $\kappa = 5{,}9$) at different scales ($2m \times 2m$, $60m \times 60m$, $300m \times 300m$) were generated for percolation analysis. The percolation thresholds obtained from Eq. 24 and numerical simulations are depicted in Fig. 15. The remarkable concurrence between the predicted thresholds and the simulation outcomes underscores the robust performance of the derived relationships (Eq. 24) in accurately forecasting percolation thresholds across diverse parameter configurations and study scales for DFNs.

https://doi.org/10.5194/egusphere-2025-2440
Preprint. Discussion started: 17 June 2025

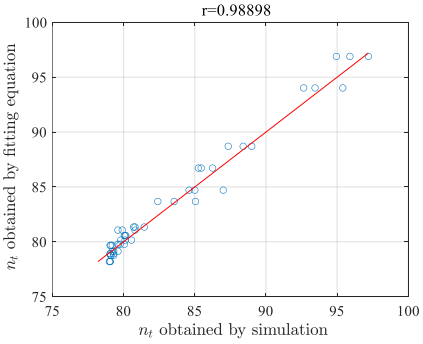

Fig. 15: Validation of Eq. 24 in study areas on different scales.

4.2 Comparison with analytical solutions of simple fracture networks

The equations derived in Section 3.2 are for stochastic fracture networks with fracture lengths that follow an exponential distribution and fracture orientations that follow a von-Mises distribution. Because of the complexity of such fracture networks, there is no analytical solution for the corresponding percolation threshold. However, for simple fracture networks, where both fracture location and orientation follow completely random distributions and the fracture length is identical, the analytical solution for the percolation threshold of fracture length is (Balberg et al., 1984; Berkowitz, 1995):

$$L_C = 4.2/\sqrt{\pi\rho}, \tag{25}$$

where ρ is the fracture density (=P20) calculated as $\rho = n/y^2$ and y^2 is the area of the study region. For the case of varying fracture length, the corresponding threshold is:

$$\bar{L}_t = \sqrt{L_C^2 - \sigma^2}, \tag{26}$$

where σ^2 is the variance of fracture length distribution. If the length follows an exponential distribution with parameter λ, Eq. 26 becomes (Berkowitz, 1995). Therefore, this section utilises fracture networks characterized by an exponential distribution of fracture lengths as a case study to compare the derived thresholds with analytical solutions.

$$\bar{L}_t = L_C/\sqrt{2} = 4.2/\sqrt{\frac{2\pi n}{y^2}} \approx 1.676\, y n^{-0.5}, \tag{27}$$

This is a special case covered by the relationships derived in this work by setting $\kappa = 0$ for a completely random distribution of fracture orientation and ignoring $\cos\Delta$ as it is now irrelevant. Eq. 16 then becomes:

$$\bar{L}_{ts} = y\, a_{32} n^{b_{33}}, \tag{28}$$

where $a_{32} = 0.9823$, $b_{33} = -0.4730$ The equation can be further simplified to:

$$\bar{L}_{ts} = 0.9823 y n^{-0.4730}, \tag{29}$$

https://doi.org/10.5194/egusphere-2025-2440
Preprint. Discussion started: 17 June 2025

which should be compared to Eq. 27. Note that the difference between the two equations is due to the different probabilities used to derive the percolation threshold. The theoretical solution is for a percolation probability of 50% while the derived relationship is for a percolation probability of 0%, as discussed above, and therefore it should be smaller.

There is a striking similarity between the analytical solution for p50 and the solution we derived for p0. The reasons why these two equations are so similar and what the factor of two in the first coefficient represents are important. These will be discussed in future work instead of here since it is not the focus of this work.

To compare the solutions, fracture networks with $n = 100, 200, 300, 400$ and 500 in a square of $75m \times 75m$ are used for the simulations. Percolation thresholds corresponding to $p0$, $p50$ and $p100$ are calculated by Monte Carlo simulations and the results are shown in Figure 16. As demonstrated, the analytical solution is close to the $p50$ percolation threshold with an average absolute difference of 4.9%. On the other hand, the solution based on the derived equation is close to that of $p0$ with an average absolute difference of 11.4%.

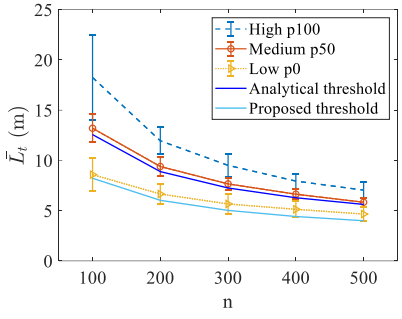

Figure 16: Comparison of percolation thresholds determined by the analytical solution, the derived equation, and numerical simulations. The points are the averages of 20 groups of MC simulations and the error bars are three times the corresponding standard deviations.

4.3 Percolation analysis of real fracture networks using the derived equation

Two real fracture networks, as shown in Figure 17a and Figure 18a, are used to demonstrate further the application of the derived percolation threshold equations. Figure 17a shows a set of fractures traces on a rock outcrop taken from Wilson (Wilson, 2001). Figure 18a are fracture traces in the deformation bands on the Valley of Fire State Park, Nevada (Barton, Hsieh, 1989). Mid-points of the fractures are used to represent the fracture locations, as shown in Figure 17b and Figure 18b, respectively. They are all considered to follow approximately the Poisson distribution. The number of fractures, n, in the three systems are 35, 186. Clearly there is one dominant direction of fracture orientations in these systems, as illustrated in the rose diagrams shown in Figure 17c and Figure 18c. The orientation dispersion parameters (κ) were calculated to be 145.18 and 25.68. For fracture length, the histogram in Figure 17d indicates an approximately exponential distribution for the first fracture set. For

https://doi.org/10.5194/egusphere-2025-2440
Preprint. Discussion started: 17 June 2025

the second and third sets, the histograms (Figure 18d) suggest lognormal distributions. The average fracture lengths $\bar{L}$ are 0.249m, 0.282mm, 0.9544m and the side lengths y of study areas are 2.5m, 8mm, 7m, respectively.

Using Eqs. 23 and 24 with the parameters $(\bar{L}, v, \Delta, \kappa)$ listed in Table 7, the calculated percolation thresholds $(y_n \times n_t)$ in the horizontal and vertical directions can be calculated. For Figure 17a, the calculated percolation thresholds are 126 (horizontal) and 94 (vertical). The threshold in the horizontal direction is much greater than that in the vertical direction due to the fact that fractures are mainly vertical in this case. The fracture numbers are all less than these two thresholds hence the fracture network is not percolated in both directions. This conclusion can easily be confirmed in this case by visual inspection of the fracture system displayed in Figure 17a.

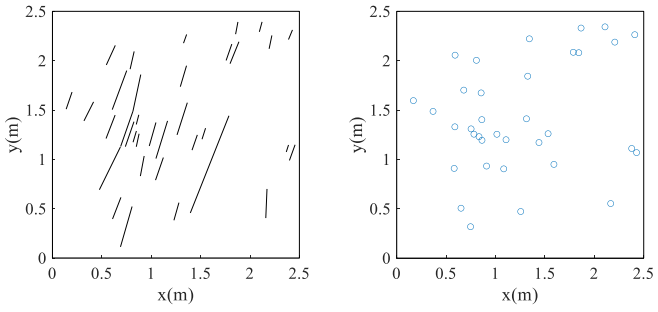

(a) Fracture network from an outcrop (b) Fracture centres

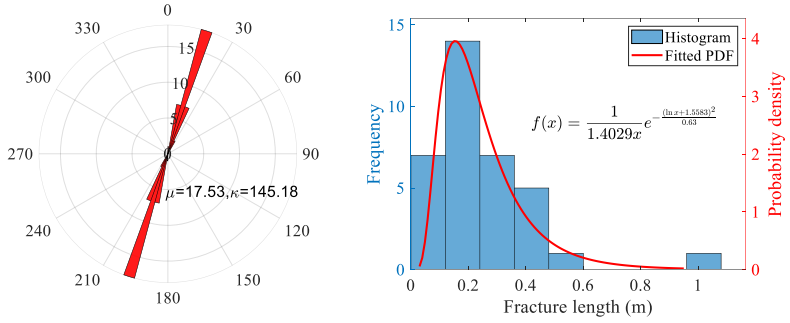

(c) Fracture orientation (d) Fracture length

Figure 17: A set of fractures from an outcrop (Wilson, 2001) and the network properities.

Table 7: Parameters of three real fracture networks in Figure 17a and percolation assessment.

Direction	N	$\Delta(°)$	v	κ	$\bar{L}$	y	$y_n \times n_t$	$N \geq y_n \times n_t$	Percolated
Horizontal	35	72.47	0.18	145.18	$0.25m$	$2.5m$	126	No	No

https://doi.org/10.5194/egusphere-2025-2440
Preprint. Discussion started: 17 June 2025

Vertical	35	17.53	0.18	145.18	$0.25m$	$2.5m$	94	No	No

For the fracture set (Figure 18a), the average fracture length is $1.19m$. The horizontal percolation threshold $y \times \bar{L}_t$ is $1.34m$ and the vertical threshold is $0.69m$. The average fracture length in this case is greater than the vertical threshold and therefore the fracture network is percolated vertically but not horizontally. On close inspection of Figure 18a, there is a cluster of fractures (marked in red) connecting the top and bottom sides of the study region.

Table 8: Parameters of three real fracture networks in Figure 18a and percolation assessment.

Direction	N	$\Delta(°)$	κ	y	$\bar{L}$	$y \times \bar{L}_t$	$\bar{L} \geq y \times \bar{L}_t$	Percolated
Horizontal	146	80.54	25.68	$7m$	$1.19m$	$1.34m$	No	No
Vertical	146	9.46	25.68	$7m$	$1.19m$	$0.69m$	Yes	Yes

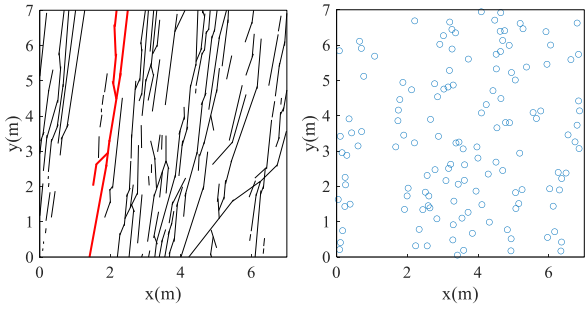

(a) Fracture network from an outcrop (b) Fracture centres

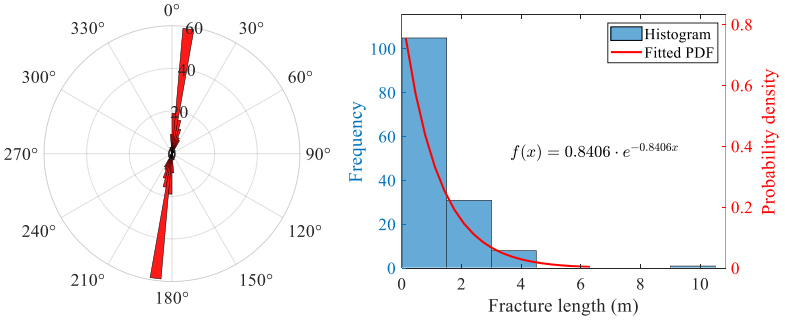

(c) Fracture orientation (d) Fracture length

Figure 18: Fracture traces of deformation bands in the Valley of Fire State Park, Nevada (Barton, Hsieh, 1989) and the corresponding network properties.

https://doi.org/10.5194/egusphere-2025-2440
Preprint. Discussion started: 17 June 2025

5 Conclusions

Percolation analysis of fracture networks is important for many applications, including oil and gas recovery, geothermal energy exploitation, hydrology, and groundwater protection in radioactive waste storage. In this paper, we focus on the percolation threshold relevant to rock impermeability, which is critically important for the safe underground storage of waste and energy materials.

Our approach to the calculation of the percolation threshold makes direct use of the characteristic parameters of 2D fracture network, in particular the number of fractures n, the fracture size (length) $\bar{L}$ and the fracture orientation Δ. This differs from the simplified approaches of using indirect characteristic parameters (e.g., fractal dimension), which could produce misleading results because fracture orientation is not considered. The assessment of fracture networks in this research was made under the following assumptions: (1). the centre points of fractures are randomly and independently distributed in space; (2). the lengths of fractures follow an exponential distribution; and (3). the orientations of fractures follow a von-Mises distribution, the parameters of which are the mean orientation μ and the concentration parameter κ. The relationship between fracture network parameters and the corresponding percolation threshold is obtained from a large number of simulations. A non-linear multivariate fitting process was used to derive the final prediction equation for the percolation threshold in the form of $\bar{L}_t = f(n, cos\Delta, \kappa)$. The derived equation provides a reliable relationship and an efficient way to estimate the connectivity and percolation state of a fracture network based directly on its parameters. The relationship was cross-validated using a published analytical solution and was further applied to three real fracture networks. The results demonstrate that the derived relationship can be used for fracture networks at different scales using a rescaling coefficient and can also be used for the assessment of percolation in different directions. The derived relationship is a useful extension for rock impermeability evaluation (zero probability percolation p0), compared with the commonly used percolation assessment based on excluded volume, which corresponds only to the occurrence of percolation on average (i.e., 50% probability percolation, p50). Additionally, this work also studies fracture network models with log-normally distributed fracture lengths and derives zero percolation formulas, reaching conclusions similar to those mentioned above.

Due to the complexity of multiple sets of fractures, the work only is limited to 2D fracture network with a single set. In future work, the work will be extended to cover 2D and 3D fracture systems with multiple sets of fractures.

Data Availability Statement

All the numerical simulation results are open-sourced and available at the Mendeley Data doi: 10.17632/y7yw25brph.1.

Declaration of interests

The authors declare that they have no known competing financial interests or personal relationships that could have appeared

https://doi.org/10.5194/egusphere-2025-2440
Preprint. Discussion started: 17 June 2025

563 to influence the work reported in this paper.

564 **Redit authorship contribution statement**

565 Shaoqun Dong: Writing - original draft, Methodology, Conceptualization, Supervision, Investigation. Lianbo Zeng: Writing -
566 review & editing, Validation, Methodology, Supervision. Chaoshui Xu: Writing - review & editing, Conceptualization,
567 Supervision, Validation. Peter Dowd: Writing - review & editing, Methodology, Investigation. Tao Wang: Investigation,
568 Validation, Conceptualization. Wenya Lyu: Investigation, Validation. Guohao Xiong: Validation, Investigation.

569 **Acknowledgement**

570 We would like to express our sincere gratitude to the Editors, Dr. Sean McKenna, and the anonymous reviewers for their
571 thorough review and insightful comments, which have greatly improved the quality of this paper.
572 This work was financially supported by the Fundamental Research Funds for the National Natural Science Foundation of
573 China (Grant No. 42002134), China Postdoctoral Science Foundation (Grant No. 2021T140735), Science Foundation of China
574 University of Petroleum, Beijing (Grant No. 2462024YJRC013), and China Scholarship Council. The work was undertaken
575 while the first author was a China Scholarship Council Visiting Scholar at the University of Adelaide.
576

577 **Reference**

578 Alghalandis, Y. F., Dowd, P. A., and Xu, C.: Connectivity Field: A Measure for Characterising Fracture Networks. Math.
579 Geosci., 47(1), 63-83, doi:10.1007/s11004-014-9520-7, 2015.
580 Ali, A. and Jakobsen, M.: Seismic characterization of reservoirs with multiple fracture sets using velocity and attenuation
581 anisotropy data, J. Appl. Geophys., 75(3), 590-602, doi:1 0.1016/j.jappgeo.2011.09.003, 2011.
582 Balberg, I., Anderson, C. H., Alexander S., and Wagner N.: Excluded volume and its relation to the onset of percolation. Phys.
583 Rev. B, 30(7), 3933, doi:10.1103/PhysRevB.30.3933, 1984.
584 Balberg, I. and Binenbaum, N.: Computer study of the percolation threshold in a two-dimensional anisotropic system of
585 conducting sticks, Phys. Rev. B, 28(7), 3799-3812, doi:10.11 03/PhysRevB.28.3799, 1983.
586 Barker, J. A.: Intersection statistics and percolation criteria for fractures of mixed shapes and sizes, Comput. Geosci., 112, 47-
587 53, doi:10.1016/j.cageo.2017.12.001, 2018.
588 Barton, C. C. and Hsieh, P. A.: Physical and hydrologic-flow properties of fractures, United States of America: American
589 Geophysical Union, America, 1989.
590 Berkowitz, B.: Analysis of fracture network connectivity using percolation theory, Math. Geosci., 27(4), 467-483,
591 doi:10.1007/BF02084422, 1995.

https://doi.org/10.5194/egusphere-2025-2440
Preprint. Discussion started: 17 June 2025

592 Bour, O. and Davy, P.: On the connectivity of three-dimensional fault networks, Water Resour. Res., 34(10), 2611-2622,
593 doi:10.1029/98WR01861, 1998.
594 Bour, O. and Davy, P.: Connectivity of random fault networks following a power law fault length distribution, Water Resour.
595 Res., 33(7), 1567-1583, doi:10.1029/96WR00433, 1997.
596 Catapano, E., Cassé, M., and Ghibaudo, G.: Cryogenic MOSFET Subthreshold Current: From Resistive Networks to
597 Percolation Transport in 1-D Systems, IEEE Transactions on Electron Devices, 70(8), 4049-4054,
598 doi:10.1109/TED.2023.3283941, 2023.
599 Charlaix, E., Guyon, E., and Rivier, N.: A criterion for percolation threshold in a random array of plates, Solid State Commun,
600 50(11), 999-1002, doi:10.1016/0038-1098(84)90274-6, 1984.
601 de Dreuzy, J., Davy, P., and Bour O.: Percolation parameter and percolation-threshold estimates for three-dimensional random
602 ellipses with widely scattered distributions of eccentricity and size, Phys. Rev. E, 62(5), 5948-5952,
603 doi:10.1103/PhysRevE.62.5948, 2000.
604 Dogan, M. O.: Extended Multiple Interacting Continua (E-MINC) Model Improvement with a K-Means Clustering Algorithm
605 Based on an Equi-dimensional Discrete Fracture Matrix (ED-DFM) Model, Math. Geosci., doi:10.1007/s11004-023-10110-9,
606 2023.
607 Dong, S., Lyu, W., Xia, D., Wang, S., Du, X., Wang T, Wu Y., and Guan C..: An approach to 3D geological modeling of
608 multi-scaled fractures in tight sandstone reservoirs, Oil and Gas Geology, 41(3), 627-637, doi:10.11743/ogg20200318, 2020.
609 Dong, S., Wang, T., Zeng, L., Liu, K., Liang, F., Yin, Q., and Cao D.: Analysis of relationship between underground space
610 percolation and fracture properties, Earth Science Frontiers, 3(26), 140-146. doi:10.13745/j.esf.sf.2019.4.22, 2019.
611 Dong, S., Wang, Z., and Zeng, L.: Lithology identification using kernel Fisher discriminant analysis with well logs, Geoenergy
612 Sci. Eng., 143, 95-102, doi:10.1016/j.petrol.2016.02.017, 2016.
613 Dong, S., Zeng, L., Cao, H., Xu, C., and Wang, S.: Principle and implementation of discrete fracture network modeling
614 controlled by fracture density, Geol. Rev., 64(5), 1302-1314, doi: 10.16509/j.georeview.2018.05.020, 2018.
615 Dong, S., Zeng, L., Dowd, P., Xu, C., and Cao, H.: A fast method for fracture intersection detection in discrete fracture
616 networks, Comput. Geotech., 98, 205-216, doi:10.1016/j.compgeo.20 18.02.005, 2018.
617 Dong, S., Zeng, L., Du, X., Bao, M., Lyu, W., Ji, C., and Hao J.: An intelligent prediction method of fractures in tight carbonate
618 reservoirs, Petroleum Exploration and Development, 49(6), 1179-1189, doi:10.11698/PED.2 0220367, 2022.
619 Dong, S., Zeng, L., Xu, C., Cao, H., Wang, S., and Lyu, W.: Some progress in reservoir fracture stochastic modeling research,
620 Oil Geophysical Prospecting, 53(3), 30-51, doi:10.13810/j.cnki. issn.1000-7210.2018.03.023, 2018.
621 Dowd, P. A., Xu, C., Mardia, K. V., and Fowell, R. J.: A Comparison of Methods for the Stochastic Simulation of Rock
622 Fractures, Math. Geosci., 39(7), 697-714, doi:10.1007/s11004-007-9116-6, 2007.
623 Einstein, H. H. and Locsin, J.: Modeling rock fracture intersections and application to the Boston Area, J. Geotech. Geoenviron.,

https://doi.org/10.5194/egusphere-2025-2440
Preprint. Discussion started: 17 June 2025

624 11(138), 1415-1421, doi:10.1061/(ASCE)GT.1943-5606.0 000699, 2012.
625 Fadakar Alghalandis, Y.: ADFNE: Open source software for discrete fracture network engineering, two and three dimensional
626 applications, Comput. Geosci., 102, 1-11. doi:10.1016/j.cag eo.2017.02.002, 2017.
627 Huseby, O. and Thovert, J. F.: Geometry and topology of fracture systems, Journal of Physics A: Mathematical and General,
628 30(5), 1415, doi:10.1088/0305-4470/30/5/012, 1997.
629 Jafari, A. and Babadagli, T.: Relationship between percolation–fractal properties and permeability of 2-D fracture networks,
630 Int. J. Rock. Mech. Min., 60, 353-362, doi:10.1016/j.ijrm ms.2013.01.007, 2013.
631 Jafari, A. and Babadagli, T.: A sensitivity analysis for effective parameters on 2D fracture-network permeability, SPE Reserv.
632 Eval. Eng., 12(3), 455-469, 2009.
633 Khamforoush, M. and Shams, K.: Percolation thresholds of a group of anisotropic three-dimensional fracture networks,
634 Physica. A., 385(2), 407-420, doi:10.1016/j.physa.2007.07.037, 2007.
635 Khamforoush, M., Shams, K., Thovert, J. F. and Adler, P. M.: Permeability and percolation of anisotropic three-dimensional
636 fracture networks, Phys. Rev. E, 77(5), 56307, doi:10.1103/PhysRev E.77.056307, 2008.
637 Kolyukhin, D.: Sensitivity analysis of discrete fracture network connectivity characteristics, Math. Geosci., 54(1), 225-241,
638 doi:10.1007/s11004-021-09966-6, 2022.
639 Liu, R., Zhu, T., Jiang, Y., Li, B., Yu, L., Du, Y., and Wang Y.: A predictive model correlating permeability to two-dimensional
640 fracture network parameters, B. Eng. Geol. Environ., 78(3), 1589-1605, doi:10.1007/s10064-018-1231-8, 2019.
641 Manzocchi, T.: The connectivity of two-dimensional networks of spatially correlated fractures, Water Resour. Res., 38(9),
642 1162, doi:10.1029/2000WR000180, 2002.
643 Manzocchi, T., Walsh, D. A., Carneiro, M., and López-Cabrera, J.: Compression-based Facies Modelling, Math. Geosci., 55(5),
644 625-644, doi:10.1007/s11004-023-10048-y, 2023.
645 Mardia, K. V., Nyirongo, V. B., Walder, A. N., Xu, C., Dowd, P. A., Fowell, R. J., and Kent J. T.: Markov Chain Monte Carlo
646 implementation of rock fracture modelling, Math. Geosci., 39(4), 355-381, http://d oi.org/10.1007/s11004-007-9099-3, 2007.
647 Masihi, M. and King, P. R.: A correlated fracture network: Modeling and percolation properties, Water Resour. Res., 43(7),
648 doi:10.1029/2006WR005331, 2007.
649 McKenna, S. A., Akhriev, A., Echeverría Ciaurri, and D., Zhuk, S.: Efficient Uncertainty Quantification of Reservoir
650 Properties for Parameter Estimation and Production Forecasting, Math. Geosci., 52(2), 233-251, doi:10.1007/s11004-019-
651 09810-y, 2020.
652 Mourzenko, V. V., Thovert, J. F., and Adler, P. M.: Macroscopic permeability of three-dimensional fracture networks with
653 power-law size distribution, Phys. Rev. E, 69(6), 66307, doi:10.1103/Ph ysRevE.69.066307, 2004.
654 Mourzenko, V. V., Thovert, J., and Adler, P. M.: Percolation and permeability of fracture networks in excavated damaged
655 zones, Phys. Rev. E, 86(2), 26312, doi:10.1103/PhysRevE.86. 026312, 2012.

https://doi.org/10.5194/egusphere-2025-2440
Preprint. Discussion started: 17 June 2025

656 Mourzenko, V. V., Thovert, J., and Adler, P. M.: Percolation and permeability of three dimensional fracture networks with a
657 power law size distribution, Fractals in Engineering, 81-95, doi:10.1007 /1-84628-048-6_6, 2005.
658 Ngia, L. S. H. and Sjoberg, J.: Efficient training of neural nets for nonlinear adaptive filtering using a recursive Levenberg-
659 Marquardt algorithm. IEEE T. Signal. Proces., 48(7), 1915-1927. http:// doi.org/10.1109/78.847778, 2000.
660 Or, D., Furtak-Cole, E., Berli, M., Shillito, R., Ebrahimian, H., Vahdat-Aboueshagh, H., and McKenna S. A.: Review of
661 wildfire modeling considering effects on land surfaces, Earth-Sci. Rev., 245, 104-569, doi:10.1016/j.earscirev.2023.104569,
662 2023.
663 Rizzo, R. E., Healy, D., Heap, M. J., and Farrell, N. J.: Detecting the Onset of Strain Localization Using Two-Dimensional
664 Wavelet Analysis on Sandstone Deformed at Different Effective Pressures, J. Geophys. Res-sol. Ea., 123(12), 10, 410-460,
665 478, doi:10.1029/2018JB015898, 2018.
666 Robinson, P. C.: Connectivity of fracture systems-a percolation theory approach, J. Phys. A: Math. Gen., 16(3), 605.
667 doi:10.1088/0305-4470/16/3/020, 1983.
668 Shokri, A. R., Babadagli, T., and Jafari, A.: A critical analysis of the relationship between statistical- and fractal-fracture-
669 network characteristics and effective fracture-network permeability, SPE Reserv. Eval. Eng., 19(3), 494-510,
670 doi:10.2118/181743-PA, 2016.
671 Sun, H., Radicchi, F., Kurths, J., and Bianconi, G.: The dynamic nature of percolation on networks with triadic interactions,
672 Nat. Commun., 14(1), doi:10.1038/s41467-023-37019-5, 2023.
673 Tang, H., Zhao, Y., Kang, Z., Lv, Z., Yang, D., and Wang, K.: Investigation on the Fracture-Pore Evolution and Percolation
674 Characteristics of Oil Shale under Different Temperatures, Energies, 15(10), 3572, doi:10.3390/en15103572, 2022.
675 Thovert, J. F., Mourzenko, V. V., and Adler, P. M.: Percolation in three-dimensional fracture networks for arbitrary size and
676 shape distributions, Phys. Rev. E, 95(4), 42112, doi:10.1103/Phy sRevE.95.042112, 2017.
677 Walsh, D. A. and Manzocchi, T.: Connectivity in Pixel-Based Facies Models. Math. Geosci., 53(3), 415-435.
678 doi:10.1007/s11004-021-09931-3, 2021.
679 Wei, Y., Dong, Y., Yeh, T. J., Li, X., Wang, L., and Zha, Y.: Assessment of uncertainty in discrete fracture network modeling
680 using probabilistic distribution method, Water Science and Technology, 76(9-10), 2802, doi:10.2166/wst.2017.451, 2017.
681 Wilson, T. H.: Scale Transitions in Fracture and Active Fault Networks, Math. Geosci., 33(5), 591-613,
682 doi:10.1023/A:1011096828971, 2001.
683 Xu, C. and Dowd, P.: A new computer code for discrete fracture network modelling. Comput. Geosci., 36(3), 292-301.
684 doi:10.1016/j.cageo.2009.05.012, 2010.
685 Xu, C., Dowd, P., Mardia, K. V., and Fowell, R. J.: A connectivity index for discrete fracture networks, Math. Geosci., 38(5),
686 611-634, doi:10.1007/s11004-006-9029-9, 2007.
687 Yao, C., Shao, Y., Yang, J., Huang, F., Hem, C., Jiang, Q., and Zhou C.: Effects of fracture density, roughness, and percolation

https://doi.org/10.5194/egusphere-2025-2440
Preprint. Discussion started: 17 June 2025

of fracture network on heat-flow coupling in hot rock masses with embedded three-dimensional fracture network, Geothermics, 87, 101846, doi:10.1016/j.geotherm ics.2020.101846, 2020.

Yi, Y. and Tawerghi, E.: Geometric percolation thresholds of interpenetrating plates in three-dimensional space, Phys. Rev. E, 79(4), 41134, doi:10.1103/PhysRevE.79.041134, 2009.

Zeng, L., Gongm, L., Guan, C., Zhang, B., Wang, Q., Zeng, Q., and Lyu W.: Natural fractures and their contribution to tight gas conglomerate reservoirs: A case study in the northwestern Sichuan Basin, China, J. Petrol. Sci. Eng., 210, 110028, doi:10.1016/j.petrol.2021.110028, 2022.

Zhao, W. and Hou, G.: Fracture prediction in the tight-oil reservoirs of the Triassic Yanchang Formation in the Ordos Basin, northern China, Petrol. Sci., 14(1), 1-23, doi:10.1007/s12182-016-0141-2, 2017.

Zhao, Y., Feng, Z., Liang, W., Yang, D., Hu, Y., and Kang, T.: Investigation of fractal distribution law for the trace number of random and grouped fractures in a geological mass, Eng. Geol., 109(3-4), 224-229, doi:10.1016/j.enggeo.2009.08.002, 2009.

Zhao, Y., Feng, Z., Lv, Z., Zhao, D., and Liang, W.: Percolation laws of a fractal fracture-pore double medium, Fractals, 24(04), 1650053, doi:10.1142/S0218348X16500535, 2016.

Zhu, W., He, X., Khirevich, S., Patzek, and T. W.: Fracture sealing and its impact on the percolation of subsurface fracture networks., Geoenergy Sci. Eng., 218, 111023, doi:10.1016/j.petro l.2022.111023, 2022.